RESEARCH PAPER

Displacement Analysis of a Piezoelectric Based Multi-layered Micropump Diaphragm

Hamid Asadi Dereshgi[1] · Mustafa Zahid Yildiz[2] · Huseyin Dal[3]

Abstract

This paper presents the diaphragm displacement analysis of multi-layered circular piezoelectric actuator (MCPA) using analytical, numerical and experimental methods. The piezoelectric zirconate titanate (PZT) actuator model examined in this study consists of a structure with 3 different diameters and 7 layers. The multi-layered and multi-covered actuator model was composed of three main layers in different radii and thickness with silicon, brass and the PZT and four additional layers with silver and bonding. When creating an analytical model, the effects of all layers were taken into account on the static deflection performance of the actuator. The classical laminated plate theory based on Kirchhoff thin plate theory was used in the analytic modelling studies of the actuator. The mathematical model, which is the solution of the static displacement equation of the non-homogenous for the MCPA of the micropump, depends on the applied voltage and pressure load together with the material and physical properties. The electric-solid coupling of the piezoelectric actuator and the silicon diaphragm layer under the effect of applied voltage load, and the silicon-fluid coupling under the uniform fluid pressure were simulated by numerical modelling with finite elements. In addition, the maximum displacements of the MCPA with silicon exposed to uniform flow pressure and electric voltage load were measured at different frequencies experimentally. It was observed that the results obtained from the analytical model, finite element analysis and experimental studies were sufficiently compatible with each other. Using the verified analytical model, the effects of layer thicknesses, layer diameters and adhesive layer on actuator static displacement performance are discussed.

Keywords Piezoelectric actuator · Micropump actuator · Silicon diaphragm · Circular plate · Classical laminated plate theory

List of Symbols

PZT	Piezoelectric zirconate titanate
MCPA	Multi-layered circular piezoelectric actuator
MEMS	Microelectromechanical systems
r, θ, z	The polar coordinate components
R	The radius of the layer
R_i, R_m, R_o	Radius of centre actuator, middle and outer annular actuator, respectively
d_{31}	The piezoelectric constant
$\sigma_r, \sigma_\theta, \tau_{rz}$	Radial, angular and shear stress, respectively
t_i	Thickness of ith layer
t_s	Thickness of the silicon layer
t_{br}	Thickness of the brass layer
t_{pzt}	Thickness of the PZT layer
u, w	Lateral and transverse displacements, respectively
$\varepsilon_r, \varepsilon_\theta$	Radial and tangential strains
E_z	Electric field strength of the PZT layer
V	Electric voltage
E_i	Young's modulus of the layer
E_{pzt}	Young's modulus of the PZT layer
μ	Poisson ratio of the layer
s_{xx}^E	Piezoelectric elastic compliance constant
N_r, N_θ	Radial and tangential forces, respectively
M_r, M_θ	Radial and tangential forces, respectively
D_1, D_2, D_3	The bending stiffness matrix of the actuator
Q_r	Shear force along the vertical direction
P	Uniform static pressure

✉ Hamid Asadi Dereshgi
hamidasadi@arel.edu.tr

1. Department of Biomedical Engineering, Istanbul Arel University, 34537 Istanbul, Turkey

2. Department of Electrical and Electronics Engineering, Sakarya University of Applied Sciences, 54050 Sakarya, Turkey

3. Department of Mechanical Engineering, Sakarya University, 54050 Sakarya, Turkey

Springer

1 Introduction

Micropumps can be used to transfer small volumes of fluids in applications such as microelectronics cooling (Singhal and Garimella 2007; Dereshgi 2019), medical systems (Doll et al. 2004; Yildiz and Dereshgi 2019; Dereshgi and Yildiz 2019; Ramesh et al. 2019), chemical (Kim et al. 2004), biological (Jang and Lee 2000) and others (Zordan et al. 2009; Wang et al. 2009). Therefore, they have attracted the attention of industrial researchers and consumers (Munas et al. 2015). Micropumps according to the physical mechanism are divided into two types, namely mechanical and non-mechanical micropumps (Abhari et al. 2012; Dereshgi et al. 2020a). In the structure of mechanical micropump are moving mechanical parts, such as pumping diaphragms and check valves. By contrast, in the structure of non-mechanical micropumps are not any mechanical parts to move the fluid. In these micropumps, the flow rate is obtained by hydrodynamic, electroosmosis or electrowetting effects (Wang and Fu 2018). According to the literature survey, mechanical micropumps are more suitable for medical applications than non-mechanical micropumps. In non-mechanical micropumps, the fluid is affected by magnetic field, electric field, acoustic field or heat. The methods used to transfer fluid in non-mechanical micropumps may change the chemical properties of the drug. In mechanical micropumps, fluid pumping is performed by physical actuators. The most common physical actuators include piezoelectric (Afrasiab et al. 2011; Kolahdouz et al. 2014; Dereshgi and Yildiz 2018a, b), electrostatic (Uhlig et al. 2018), electromagnetic (EM) (Rusli et al. 2018), electroactive polymer (EAP) (Cheong et al. 2018), thermo-pneumatic (Chee et al. 2016), thermally expandable polymer (Tripathi et al. 2017) and shape memory alloy (Guerine et al. 2018). Based on literature studies, piezoelectric can perform well compared to other mentioned actuators. They produce a reasonably intermediate pressure against low energy consumption and operate quick compared to other actuators.

In the fabricating of micropumps, it is necessary to isolate between the actuator and the fluid (Dereshgi 2016). The diaphragm material must be selected relative to the application of the micropump. Moreover, in terms of cost and resistance against abrasion should be checked. Many of the micropumps designed for biomedical applications available in open literature have chosen the diaphragm material as silicon. Because, silicon is a good biocompatible material (Nisar et al. 2008; Maillefer et al. 1999).

The theoretical modelling of the MCPA containing silicon is rather important in order to know the displacement quantity, namely to predict the voltage-flow rate relationship. Such analytical models vary depending on the design geometry according to the method of solution, the material properties that make up the MCPA, the voltage load, the fluid pressure, the fluid velocity, the mechanical properties and the parameters such as temperature. The structure of a real the MCPA consists of a three-stage structure, the passive layer at the bottom, the brass layer at the centre and the PZT layer on the top. Since it is very difficult to calculate the effect of PZT-free passive layers on other layers, analytical models of the MCPA in the literature are mostly two-stage. It is important to examine the static and dynamic behaviours since they take critical roles, and thus they are required to work very precisely. The behaviour of the piezoelectric actuators is affected by the actuator layers, fluid, and by their mechanical and electrical charge. According to the CLPT, the stress distribution along the plate thickness is assumed to be linear. Using the CLPT hypothesis, Li and Chen (2003) developed an analytical equation for the displacement of a circular piezoelectric actuator plate. They confirmed the displacement values they obtained by comparing them with the experimental results. Mo et al. (2006) investigated the static displacement behaviour of the unimorph circular diaphragm under electric charge analytically and experimentally. Other than electricity and fluid load, it is obvious that the applied mechanical load will also affect the behaviour of the actuator. Dong et al. (2007) took into account the electric field strength and the mechanical load effect for the analytical solution of the static displacement of a circular piezoelectric actuator. They stated that for maximum fluid transport, there should be an optimum thickness ratio between the PZT and metal layers. Deshpande and Saggere (2007) developed an analytical model for the static displacement of a multi-layered and two-stage circular piezoelectric actuator subjected to constant fluid pressure and voltage load, using the classical laminate plate theorem (CLPT). They verified the analytical model outputs with finite element method (FEM) and experimental study. Wang and Huo (2010) also developed the analytical static displacement model for the circular piezoelectric unimorph actuators, which were subjected to voltage load, using CLPT and verified by experimental studies. By the analytical model they established, they examined the changes in the structural parameters and material properties of the actuator.

Boundary conditions are also known to have a significant effect on the behaviour of piezoelectric actuators (Mohammadi and Abdalbeigi 2013). Optimization of the electromechanical coupling coefficient of very thin piezoelectric devices was performed by Cho et al. (2005). Analytical modelling of the nonlinear dynamic behaviour of valveless micropumps involving fluid interaction was described by Pan et al. (2001). They used the Galerkin and perturbation method for the analytical solution of the micropump under

constant pressure. Yu and Balachandran (2005) investigated the dynamic behaviour of a prestressed diaphragm. They presented a mechanical diaphragm plate model subjected to a state of plane stress. They examined the membrane-like behaviour of this diaphragm plate model and showed that the diaphragm exhibited different behaviour, such as a plate or membrane, depending on the stress value. Oniszczuk (1999) analytically solved the transverse vibration problem of the elastic layer rectangular compound membrane system using the Bernoulli Fourier method. For optimum fluid transfer of actuators, vibration frequency and modes should be determined. For this purpose, Olfatnia et al. (2010) investigated the vibrational modes and frequencies of circular piezoelectric microdiaphragms. Vibration analysis of a circular micropump diaphragm was analysed analytically and experimentally by Kaviani et al. (2014), Monemian Esfahani and Bahrami (2016), Monemian Esfahani et al. (2018) and He et al. (2017). Hu et al. (2017) theoretically, numerically and experimentally studied the vibration parameters of circular type piezo-actuators with mass.

The proposed model examined in this study is a multi-layered circular plate structure consisting of 3 main layers and 4 intermediate layers of different diameter. The MCPA model was composed of three main layers in different radii with silicon, brass and PZT. The silicon diaphragm layer is located at the bottom. The brass layer is bounded to the silicon with the adhesive layer. Piezoelectric layer consists of 4 intermediate layers: adhesive, silver, the PZT and silver layers. In most analytical models, the diameter of the PZT layer is smaller than other sub- and intermediate layers. In most of the studies, the effects of thicknesses of the bounding, diaphragm and silver layers of the micropumps on dynamic behaviour are neglected since they are very small in layers other than PZT. However, although some layers are very thin, they should have significant effects on the behaviour of the micropump performance. Therefore, in this study, the effect of all thin layers such as bounding, silver and the main layers such as PZT, brass and silicon were examined. In almost studies, since only brass and the PZT layers were

examined, 2 stepped structures were studied. In this study, in addition to the brass and the PZT layers, a larger silicon layer was added and three stepped structure was studied. It is crucial to construct a displacement model of a multi-layered that implements the actual micropump behaviour. Although it caused an important calculation load, the flexural stiffness of all layers of the circular axisymmetric unimorph PZT layered micropump diaphragm was included in the calculation. The static displacement behaviour of the MCPA under electrical voltage and uniform fluid pressure was analytically modelled and analysed. The proposed MCPA model was solved numerically by the FEM, and the results were verified by measuring the amount of displacements in experimental studies.

2 Materials and Methods

2.1 Static Displacement Modelling of the MCPA with Silicon Layer

The structure of the MCPA model is shown in Fig. 1. The silicon, brass and the PZT layers are connected by thin layers of adhesive. Based on literature studies, biocompatibility is a very important key parameter that is necessarily considered for drug delivery micropumps. Silicon is a good biocompatible material. Therefore, the silicon diaphragm has been used in the presented design. The effect of any layer of the MCPA was not neglected. The PZT layer undergoes deformation due to the reverse piezoelectric effect of the voltage load applied to the upper surface of the PZT layer. Since the PZT layer has a brittle structure, this deformation is amplified and transferred to the bottom elastic silicon layer He et al. (2017). Due to the fixed boundary conditions along the edges of the actuator, this deformation turns into transverse bending displacement in the actuator. This transverse displacement movement occurring in the silicon layer is transferred to the fluid in the lower chamber so that the fluid moves from the inlet to the outlet. The silicon layer
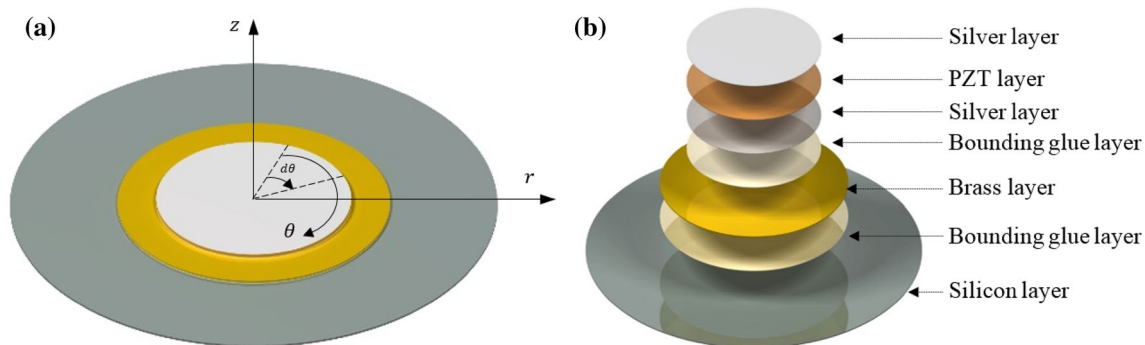

Fig. 1 The structure of the MCPA, **a** the circular coordinate system, **b** physical layer structures

located in the bottom layer of the MCPA was exposed the fixed boundary conditions throughout its circumference. The circular coordinate system was selected for analytical modelling of a MCPA with a circular geometry.

The CLPT based on Kirchhoff's thin plate theory was used to obtain closed form displacement solutions and to analytically model the multi-layered circular actuator structure subjected to uniform fluid pressure and voltage load. It is assumed that constant uniform static pressure affects the actuator in the opposite direction. The pressure applied to the actuator indicated in all text is uniform static pressure load. Accordingly, for lateral and transverse deviations of a multi-layered axial symmetry laminated actuator the general solution was obtained by the classical laminated plate theory. This MCPA consists of a uniform thickness of silicon, brass and The PZT main layers. Radiuses of silicon, brass and the PZT main layers were defined as R_i, R_m and R_o, respectively, as seen Fig. 2. The closed form of transverse displacement of the bottom silicon layer forming the MCPA can be found by the general solution. According to the CLPT, all actuator layers are perfectly bounded to each other.

The material of each layer is isotropic and obeyed the Hook's law. The thicknesses of the layers are uniform. The strain and displacements are very small and plane strain conditions are valid. The transverse shear forces on the top and bottom surfaces of each layer are close to zero. In addition, the in-plane piezoelectric (PZT-5A) constants were assumed to be transversely isotropic $(d_{31} = d_{32})$ along the poling field. In Kirchhoff's thin plate theory, σ_r, σ_θ and τ_{rz} are radial, angular and shear stresses, respectively, for small displacements.

Kinematic relations of identical layers of equal radii were defined in circular polar coordinates. The mid-plane of the silicon layer at the bottom of the piezoelectric actuator was selected as the reference plane. The z-axis was selected as the vertical axis. Each MCPA layer is sequentially located as $i = 1, 2, \ldots, n$ from the lowest silicon layer. The bottom surface of the silicon layer is the z_0 plane, and the upper surface of each layer is the z_i plane. Thus, the thickness of each layer is $t_i = z_1 - z_{i-1}$.

According to Kirchhoff's thin plate theory for polar coordinates, the radial (ε_r) and circumferential strain (ε_θ) relations of all points on the mid-plane of the reference silicon plane are as follows.

$$\varepsilon_r = \frac{\partial u_r}{\partial r} \tag{1}$$

$$\varepsilon_\theta = \frac{u_r}{r} \tag{2}$$

Here, the radial (u_r) and lateral (u_θ) displacements of the reference plane are given as;

$$u_r = -z \frac{\partial w}{\partial r} \tag{3}$$

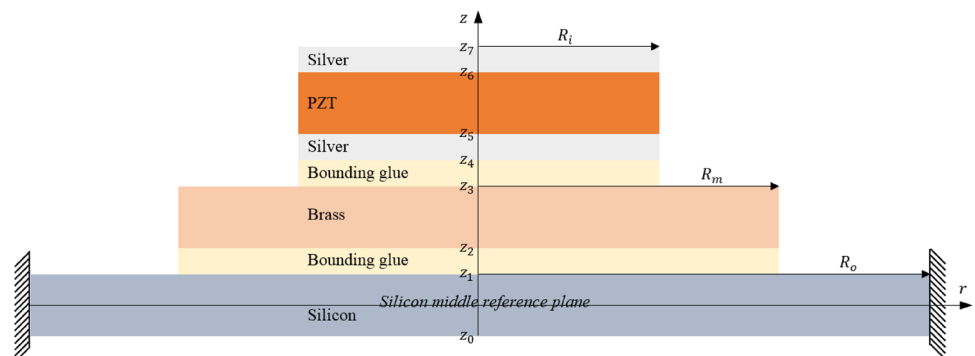$$u_\theta = -\frac{z}{r} \frac{\partial w}{\partial r} \tag{4}$$

where w is the transverse displacement of the reference plane in the vertical z direction; and θ is the transverse slope. The PZT layer of the MCPA is polarized along the vertical z-axis through its thickness. It is assumed that the electric field applied to the PZT layer of the actuator is homogeneous throughout the layer thickness.

According to the thin plate theory, in the case of axisymmetric displacement, small in-plane shear components can be negligible. Assuming a linear strain distribution along with the MCPA layers, the strain constitutive equations in terms of transverse and lateral displacements for any layer will be similar to Eq. (5).

$$\left\{ \begin{array}{c} S_r \\ S_\theta \end{array} \right\} = \left\{ \begin{array}{c} \frac{\partial u_r}{\partial r} - E_z d_{31} \\ \frac{u_r}{r} - E_z d_{31} \end{array} \right\} - z \left\{ \begin{array}{c} \frac{\partial^2 w}{\partial r^2} \\ \frac{1}{r} \frac{\partial w}{\partial r} \end{array} \right\} \tag{5}$$

where E_z is the electric field strength along the vertical z-axis and changes to $E_z = V/t_{pzt}$ depending on the applied voltage load, V is electric voltage, t_{pzt} is thickness of the PZT layer, and d_{31} is piezoelectric constant. Hence, continuity equations for radial and circumferential stress will be as in Eq. (6).

Fig. 2 Cross-sectional schematic view of the MCPA

$$\left\{ \begin{array}{c} \sigma_r \\ \sigma_\theta \end{array} \right\} = \frac{E}{1 - \mu^2} \begin{bmatrix} 1 & \mu \\ \mu & 1 \end{bmatrix} \left\{ \begin{array}{c} S_r \\ S_\theta \end{array} \right\} \tag{6}$$

where E is Young's modulus of the respective layer and μ is the Poisson's ratio of the respective layer. Young's modulus for the PZT layer is expressed by E_{pzt} that is changes to $E_{pzt} = 1/s_{11}^E$, where s_{11}^E is the elastic compliance constant for the PZT layer. The radial and circumferential force resultants N_r and N_θ are:

$$\left\{ \begin{array}{c} N_r \\ N_\theta \end{array} \right\} = D_1 \left\{ \begin{array}{c} \frac{\partial u_r}{\partial r} - E_z d_{31} \\ \frac{u_r}{r} - E_z d_{31} \end{array} \right\} - D_2 \left\{ \begin{array}{c} \frac{\partial^2 w}{\partial r^2} \\ \frac{1}{r} \frac{\partial w}{\partial r} \end{array} \right\} \tag{7}$$

The bending moments per unit length M_r and M_θ are radial, and circumferential directions are:

$$\left\{ \begin{array}{c} M_r \\ M_\theta \end{array} \right\} = D_2 \left\{ \begin{array}{c} \frac{\partial u_r}{\partial r} - E_z d_{31} \\ \frac{u_r}{r} - E_z d_{31} \end{array} \right\} - D_3 \left\{ \begin{array}{c} \frac{\partial^2 w}{\partial r^2} \\ \frac{1}{r} \frac{\partial w}{\partial r} \end{array} \right\} \tag{8}$$

Here, the bending stiffness matrix of the circular plate D_1, D_2 and D_3 is as follows.

$$D_1 = \sum_{i=1}^n \int_{z_{i-1}}^{z_i} \frac{E_i}{1 - \mu_i^2} \begin{bmatrix} 1 & \mu_i \\ \mu_i & 1 \end{bmatrix} dz \tag{9}$$

$$D_2 = \sum_{i=1}^n \int_{z_{i-1}}^{z_i} \frac{E_i z}{1 - \mu_i^2} \begin{bmatrix} 1 & \mu_i \\ \mu_i & 1 \end{bmatrix} dz \tag{10}$$

$$D_3 = \sum_{i=1}^n \int_{z_{i-1}}^{z_i} \frac{E_i z^2}{1 - \mu_i^2} \begin{bmatrix} 1 & \mu_i \\ \mu_i & 1 \end{bmatrix} dz \tag{11}$$

Equations of equilibrium in terms of the MCPA force, depending on the uniform constant pressure P, are as follows.

$$\frac{dN_r}{dr} + \frac{N_r - N_\theta}{r} = 0 \tag{12}$$

$$\frac{dQ_r}{dr} + \frac{Q_r}{r} + P = 0 \tag{13}$$

Here, Q_r is the vertical shear force in Eq. (14).

$$Q_r = \frac{dM_r}{dr} + \frac{M_r - M_\theta}{r} \tag{14}$$

The new equations are obtained by replacing Eqs. (7) and (8) in Eqs. (12) and (14), respectively.

$$D_{11} \left\{ \frac{\partial^2 u_r}{\partial r^2} + \frac{1}{r} \frac{\partial u_r}{\partial r} - \frac{u_r}{r^2} \right\} - D_{21} \left\{ \frac{\partial^3 w}{\partial r^3} + \frac{1}{r} \frac{\partial^2 w}{\partial r^2} - \frac{1}{r^2} \frac{\partial w}{\partial r} \right\} = 0 \tag{15}$$

$$D_{21} \left\{ \frac{\partial^2 u_r}{\partial r^2} + \frac{1}{r} \frac{\partial u_r}{\partial r} - \frac{u_r}{r^2} \right\} - D_{31} \left\{ \frac{\partial^3 w}{\partial r^3} + \frac{1}{r} \frac{\partial^2 w}{\partial r^2} - \frac{1}{r^2} \frac{\partial w}{\partial r} \right\} = Q_r \tag{16}$$

Here, D_{11}, D_{21} and D_{31} are as follows.

$$D_{11} = \sum_{i=1}^n \frac{E_i(z_i - z_{i-1})}{1 - \mu_i^2} \tag{17}$$

$$D_{21} = \sum_{i=1}^n \frac{E_i(z_i^2 - z_{i-1}^2)}{2(1 - \mu_i^2)} \tag{18}$$

$$D_{31} = \sum_{i=1}^n \frac{E_i(z_i^3 - z_{i-1}^3)}{3(1 - \mu_i^2)} \tag{19}$$

By evaluating Eqs. (15) and (16) together, Eqs. (20) and (21) are given as follows.

$$\frac{\partial^4 w}{\partial r^4} + \frac{2}{r} \frac{\partial^3 w}{\partial r^3} - \frac{1}{r^2} \frac{\partial^2 w}{\partial r^2} + \frac{1}{r^3} \frac{\partial w}{\partial r} = K_1 P \tag{20}$$

$$\frac{\partial^2 u_r}{\partial r^2} + \frac{1}{r} \frac{\partial u_r}{\partial r} - \frac{u_r}{r^2} = \frac{4}{r} K_3 C_3 + \frac{K_2 P r}{2} \tag{21}$$

Here, K_1, K_2 and K_3 are physical stiffness parameters and they are given in Eqs. (22), (23) and (24), respectively.

$$K_1 = \frac{D_{11}}{D_{11} D_{31} - D_{21}^2} \tag{22}$$

$$K_2 = \frac{D_{21}}{D_{11} D_{31} - D_{21}^2} \tag{23}$$

$$K_3 = \frac{D_{21}}{D_{11}} \tag{24}$$

Equation (20) shows the transverse movement of all points of the MCPA. This equation is non-homogeneous fourth-order linear ordinary differential equation. Equation (21) is a non-homogeneous second-order linear ordinary differential equation that shows the lateral movement of all points of the MCPA. The transverse and lateral general solution of the MCPA can be found as in Eqs. (25) and (26).

$$w(r) = C_1 r^2 + C_2 \ln r + C_3 r^2 \ln r + C_4 + \frac{K_1 P}{64} r^4 \tag{25}$$

$$u(r) = C_3 K_3 (2 \ln r - 1) r + C_5 r + C_6 \frac{1}{r} + \frac{K_2 P}{16} r^3 \tag{26}$$

where the integration constants C_n can be obtained by applying the corresponding boundary conditions. Note that the solutions obtained are not a function of voltage. However, the constants C_n contain physical parameters such as material properties, as well as the voltage function applied to the PZT layer. Therefore, after applying the boundary conditions, the voltage parameter will also appear in the equations. The all edges of silicon diaphragm are fully fixed at all directions (see Fig. 2). To obtain the transverse displacement of a partially covered and seven-layer actuator, the structure was divided into three steps: exterior annulus, $R_m \leq r \leq R_o$, the middle annulus, $R_i \leq r \leq R_m$ and interior core, $0 \leq r \leq R_i$ (see Fig. 3).

$$w_{ext}(r) = C_1 r^2 + C_2 \ln r + C_3 r^2 \ln r + C_4 + \frac{K_1^{ext} P}{64} r^4 \quad R_m \leq r \leq R_o \tag{27}$$

$$w_{mid}(r) = C_7 r^2 + C_8 \ln r + C_9 r^2 \ln r + C_{10} + \frac{K_1^{mid} P}{64} r^4 \quad R_i \leq r \leq R_m \tag{28}$$

$$w_{int}(r) = \frac{K_1^{int} P}{64} r^4 + C_{13} r^2 + C_{14} \ln r + C_{15} r^2 \ln r + C_{16} \quad 0 \leq r \leq R_i \tag{29}$$

$$u_{ext}(r) = C_3 K_3^{ext} r(2 \ln r - 1) + C_5 r + C_6 + \frac{K_2^{ext} P}{16} r^3 \quad R_m \leq r \leq R_o \tag{30}$$

$$u_{mid}(r) = C_9 K_3^{mid} r(2 \ln r - 1) + C_{11} r + C_{12} + \frac{K_2^{mid} P}{16} r^3 \quad R_i \leq r \leq R_m \tag{31}$$

$$u_{int}(r) = \frac{K_2^{int} P r^3}{16} + C_{15} K_3^{int} r(2 \ln r - 1) + C_{17} r + C_{18} \frac{1}{r} \quad 0 \leq r \leq R_i \tag{32}$$

Here, w_{ext}, w_{mid} and w_{int} are transverse displacements solutions of external area, middle area and centre (internal) area, respectively. u_{ext}, u_{mid} and u_{int} are lateral displacements solutions of external area, middle area and centre (internal) area, respectively. Provided that according to Hooke's law the displacement of the centre point of the actuator structure ($r = 0$), accepted to operate in the elastic region, is limited; it is required C_{14}, C_{15} and C_{18} to be zero ($C_{14} = 0, C_{15} = 0$ and $C_{18} = 0$) in Eqs. (29) and (32). The all edges of the silicon layer located in the bottom layer of the actuator are fully fixed at all directions in the analytical analysis. Transverse and lateral displacements and slopes at the edge points $r = R_o$ under fixed boundary conditions are zero. The expressions for fixed boundary conditions along the outer edges of the silicon plate at $r = R_o$ can be written as Eqs. (33)–(35).
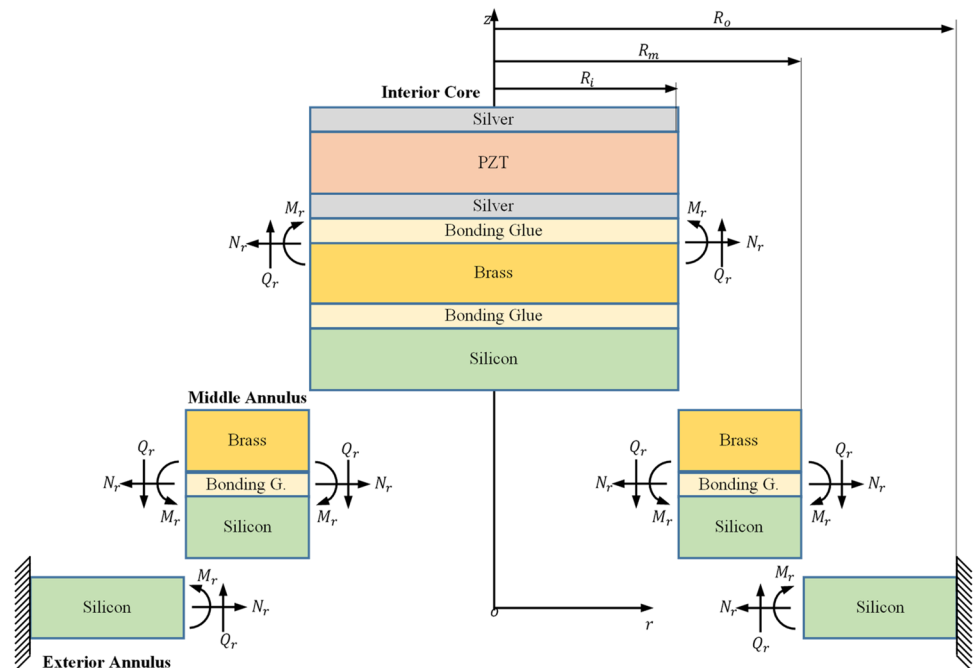
$$w_{ext}(R_o) = 0 \tag{33}$$

$$\partial w_{ext}(R_o)/\partial r = 0 \tag{34}$$

$$u_{ext}(R_o) = 0 \tag{35}$$

The equilibrium and continuity expressions at $r = R_m$ between the outer and the middle annulus;

Fig. 3 Convention for coordinate frame and the positive directions of the forces and moments

$$w_{\text{ext}}(R_{\text{m}}) = w_{\text{mid}}(R_{\text{m}}) \tag{36}$$

$$\partial w_{\text{ext}}(R_{\text{m}})/\partial r = \partial w_{\text{mid}}(R_{\text{m}})/\partial r \tag{37}$$

$$u_{\text{ext}}(R_{\text{m}}) = u_{\text{mid}}(R_m) \tag{38}$$

$$N_r^{\text{ext}}(R_{\text{m}}) = N_r^{\text{mid}}(R_{\text{m}}) \tag{39}$$

$$M_r^{\text{ext}}(R_{\text{m}}) = M_r^{\text{mid}}(R_{\text{m}}) \tag{40}$$

$$Q_r^{\text{ext}}(R_{\text{m}}) = Q_r^{\text{mid}}(R_{\text{m}}) \tag{41}$$

The equilibrium and continuity expressions at $r = R_{\text{i}}$ between the middle and the inner annulus;

$$w_{\text{mid}}(R_{\text{i}}) = w_{\text{int}}(R_{\text{i}}) \tag{42}$$

$$\partial w_{\text{mid}}(R_{\text{i}})/\partial r = \partial w_{\text{int}}(R_{\text{i}})/\partial r \tag{43}$$

$$u_{\text{mid}}(R_{\text{i}}) = u_{\text{int}}(R_{\text{i}}) \tag{44}$$

$$N_r^{\text{mid}}(R_{\text{i}}) = N_r^{\text{int}}(R_{\text{i}}) \tag{45}$$

$$M_r^{\text{mid}}(R_{\text{i}}) = M_r^{\text{int}}(R_{\text{i}}) \tag{46}$$

$$Q_r^{\text{mid}}(R_{\text{i}}) = Q_r^{\text{int}}(R_{\text{i}}) \tag{47}$$

The analytical solutions of the seven-layer and partially covered piezoelectric actuator in closed form can help to determine the static displacement behaviour under constant voltage and uniform fluid pressure. The physical parameters used to obtain the static displacement behaviour of the MCPA are given in Table 1.

All the coefficients $C_1, C_2, \ldots C_n$ can easily be solved from derivation of Eqs. (33)–(47) as below. In the later stages of the study, only transverse displacements are considered, rather than lateral displacements.

$$\left\{ \begin{array}{c} C_1 \\ C_2 \\ C_3 \\ C_4 \\ C_5 \\ C_6 \\ C_7 \\ C_8 \\ C_9 \\ C_{10} \\ C_{11} \\ C_{12} \\ C_{13} \\ C_{16} \\ C_{17} \end{array} \right\} = \left\{ \begin{array}{c} -4.43574 \times 10^{-4}P - 4.8525 \times 10^{-4}V \\ 3.1059 \times 10^{-8}P + 1.5164 \times 10^{-7}V \\ 0 \\ 1.7852 \times 10^{-7}P + 7.40315 \times 10^{-7}V \\ 8.639 \times 10^{-10}P - 1.7777 \times 10^{-8}V \\ -1.3498 \times 10^{-13}P + 2.7777 \times 10^{-12}V \\ -3.598 \times 10^{-5}P + 2.2488 \times 10^{-4}V \\ 8.7473 \times 10^{-10}P + 8.2047 \times 10^{-8}V \\ 0 \\ 1.1218 \times 10^{-8}P + 3.602 \times 10^{-7}V \\ -3.6473 \times 10^{-9}P - 2.28516 \times 10^{-8}V \\ 3.35504 \times 10^{-14}P + 3.02638 \times 10^{-12}V \\ -1.5918 \times 10^{-5}P + 1.8658 \times 10^{-3}V \\ 6.11427 \times 10^{-9}P - 1.15531 \times 10^{-7}V \\ -2.1075 \times 10^{-9}P + 9.82038 \times 10^{-8}V \end{array} \right\} \tag{48}$$
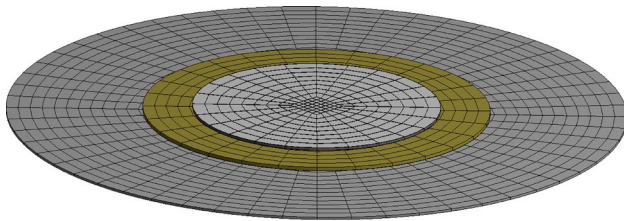
2.2 Finite Element Analysis

For the finite element analysis of the actuator, physical properties of the MCPA are given in Table 2. In this study, the mesh convergence method was used to obtain satisfactory displacement amplitude of the diaphragm where the values saturated. According to the results, the displacement reached maximum at the centre and zero at the fixed edges. Clearly, diaphragm in supply mode showed more displacement than pump mode. In contrast, the diaphragm displacement in pump mode was examined, because the diaphragm applied maximum force to the fluid in this period. In the pump mode, the diaphragm should overcome the water resistance in the chamber. However, in the supply mode, the diaphragm moves freely in the air. Therefore, deflections in both modes should not be equal. The analysis was done when the excitation input was at 5 V and 5 Hz to the piezoelectric actuator. The analysis consists of four steps in the COMSOL Multiphysics 4.3 program. The four different types of meshes were selected. The number of meshes used in first step was less than the second step, and this was repeated until the fourth step. There were 3.25% error rates between the first meshing step (normal) and the second meshing step (fine). For this micropump, the values were the very close at the second and subsequent steps. In the mesh convergence method, if the number of mesh elements

Table 1 Physical properties of the MCPA (Yang 2006; Callister and Rethwisch 2015)

	Silicon	Bonding Glue	Brass	Bonding Glue	Silver	PZT-5A
Radius (mm)	12.5	7	7	5	5	5
Thickness (μm)	100	10	140	10	10	100
Young's modulus (GPa)	162	5.17	110	5.17	40	63
Poisson ratio	0.22	0.3	0.27	0.3	0.35	0.3
$d_{31} \times 10^{-12}$ (C/N or m/V)	–	–	–	–	–	− 171

Table 2 Physical properties of PZT-5A (Yong et al. 2010)

Property	Value
Elastic compliance matrix	$\mathbf{S^E} = \begin{bmatrix} 15.0 & -5.74 & -7.22 & 0 & 0 & 0 \\ -5.74 & 15.0 & -7.22 & 0 & 0 & 0 \\ -7.22 & -7.22 & 18.8 & 0 & 0 & 0 \\ 0 & 0 & 0 & 47.5 & 0 & 0 \\ 0 & 0 & 0 & 0 & 47.5 & 0 \\ 0 & 0 & 0 & 0 & 0 & 44.3 \end{bmatrix} \times 10^{-12} \left(\frac{m^2}{N} \right)$
Piezoelectric coupling	$\mathbf{d} = \begin{bmatrix} 0 & 0 & 0 & 0 & 585 & 0 \\ 0 & 0 & 0 & 585 & 0 & 0 \\ -171 & -171 & 374 & 0 & 0 & 0 \end{bmatrix} \times 10^{-12} \left(\frac{m}{V} \right)$
Relative permittivity	$\frac{\varepsilon}{\varepsilon_0} = \begin{bmatrix} 1730 & 0 & 0 \\ 0 & 1730 & 0 \\ 0 & 0 & 1730 \end{bmatrix}, \quad \varepsilon_0 = 8.854 \times 10^{-12} \left(\frac{F}{m} \right)$

Fig. 4 FEM model of the MCPA

mentioning that the diaphragm displacement depends on the geometry and material properties of the MCPA. In this study, the diaphragm displacement was measured with a sensitivity of 0.01 μin. The experimental diaphragm displacement measurement set-up was shown in Fig. 5. However, the results of the experimental measurements of the diaphragm displacement are shown in Sect. 3.

is high, this increases the accuracy of the results. However, the analysis time will be highly increased. Therefore, it is used the second step (fine) mesh for the diaphragm displacement analysis. The finite element grid adopted to model the MCPA is shown in Fig. 4. The displacement results were given in Sect. 3. As in the analytical analysis, also in the FEM, all the edges of the silicon layer are fixed along in all directions to create fixed boundary conditions. The properties of the mesh were given in Table 3.

2.3 Experimental Analysis of Diaphragm Displacement

The diaphragm displacement was experimentally measured with a photonic sensor (MTI-2100, MTI Instruments, Albany, NY, USA). It is a fibre-optic non-contract sensor that uses reflection electronic technologies to accurately measure of diaphragm displacement. It is worth

Fig. 5 Experimental measurement set-up of diaphragm displacement

Table 3 Specifications of FEM

| Domain element statistics		Number of elements	Minimum element quality	Average element quality	Element area ratio	Maximum growth rate	Average growth rate
Our work	Normal	9976	0.08694	0.8535	0.01245	3.521	1.34
	Fine	16,832	0.1255	0.8758	0.02373	3.547	1.256
	Finer	44,268	0.1262	0.9006	0.00727	3.481	1.264
	Ext. fine	113,730	0.1262	0.9196	0.00349	3.487	1.233

3 Results and Discussions

By FEM (Fig. 6a) and experimental studies (Fig. 6b), the accuracy of the analytical solutions (Fig. 6c, d) expressing the static displacement of the multi-layered micropump actuator was studied. In the analytical studies, the variation of displacement of the midpoint and all points on the midline under the influence of different voltage (from 0 to 45 V) and uniform static pressure loads (from 0 to 400 Pa) was investigated. Because, the diaphragm was exposed to these voltage and pressure values under real operating conditions. In all calculations, it was assumed the voltage load and flow rate to be laminar in the micropump chamber and the uniform fluid pressure to remain constant. Since actuator inertia force and other dynamic effects were not taken into account in analytical modelling the frequency of the voltage in the static analysis was taken as 0 Hz. However, in the FEM and experimental studies, frequencies were between 0 and 20 Hz by 5 Hz steps. Static (DC) voltage load cannot be applied to piezoelements because the piezoelectric vertical vibration or displacement mode depends on the applied AC voltage which creates dynamic behaviour. Figure 6a shows the simulation results of diaphragm displacements at the moment of water discharge from the chamber. It shows that the increase in voltage increased displacement. Additionally, increasing the frequency reduced displacement in the range of 0-20 Hz. The displacement results have 99% liner behaviour. The maximum displacement was obtained 4.4334 μm in 45 V and 0 Hz.

Figure 6b shows the experimental results of diaphragm displacements at the discharge operation. It shows that the displacement trends were similar with FEM results at all voltage and frequencies. The displacement results have 98% liner behaviour. The maximum displacement was achieved 5.23 μm in 45 V and 5 Hz. Since diaphragm displacement was at micro-metre levels, measurement results were highly affected by environmental factors. The small differences might be because of the measurement errors, fluid movement noises in the micropump and mechanical vibrations from the experimental set-up that cannot be controlled.

Analytical solutions were obtained considering static load to the MCPA (Fig. 6c). Uniform fluid pressure and input frequency was assumed to be zero. Displacement behaviour was found to be 100% linear ($R^2 = 1$). External noises were neglected. Similarly, displacement values were increased as a function of voltage. Hereby, the displacement of the

Fig. 6 The midpoint displacement of the silicon diaphragm at 5–45 V for 0 Pa uniform static pressure, **a** FEM, **b** experiment, **c** analytical and **d** comparison of the displacement results for 0 Hz
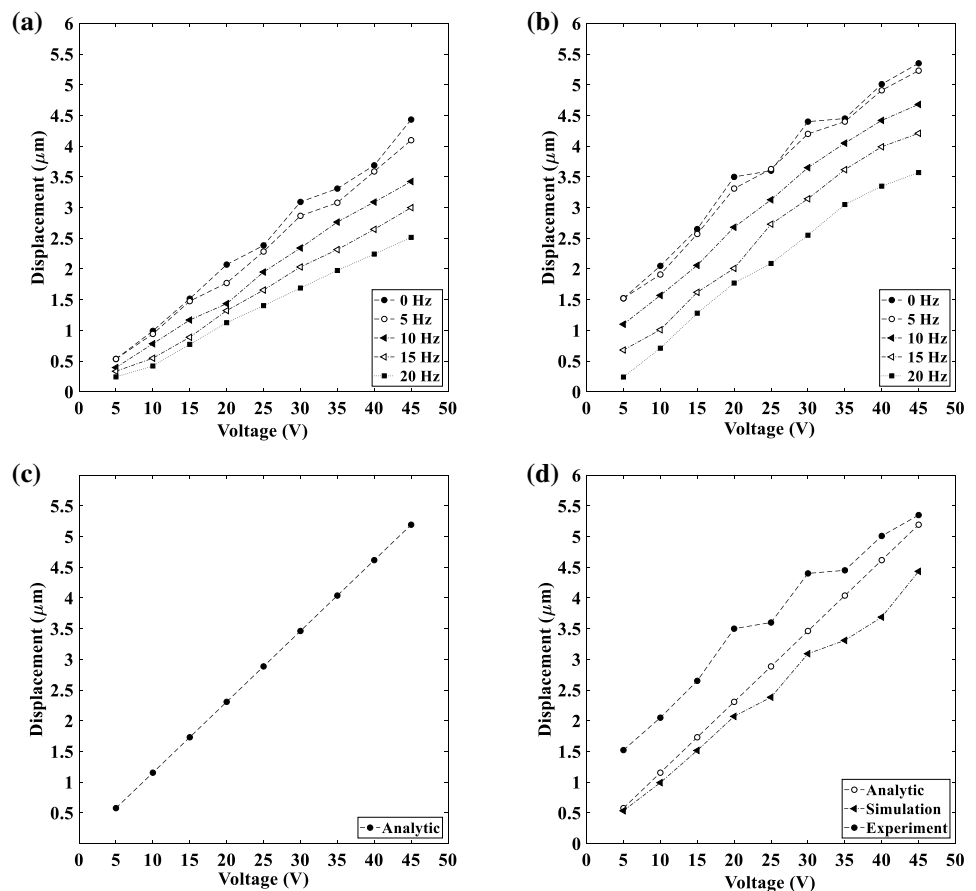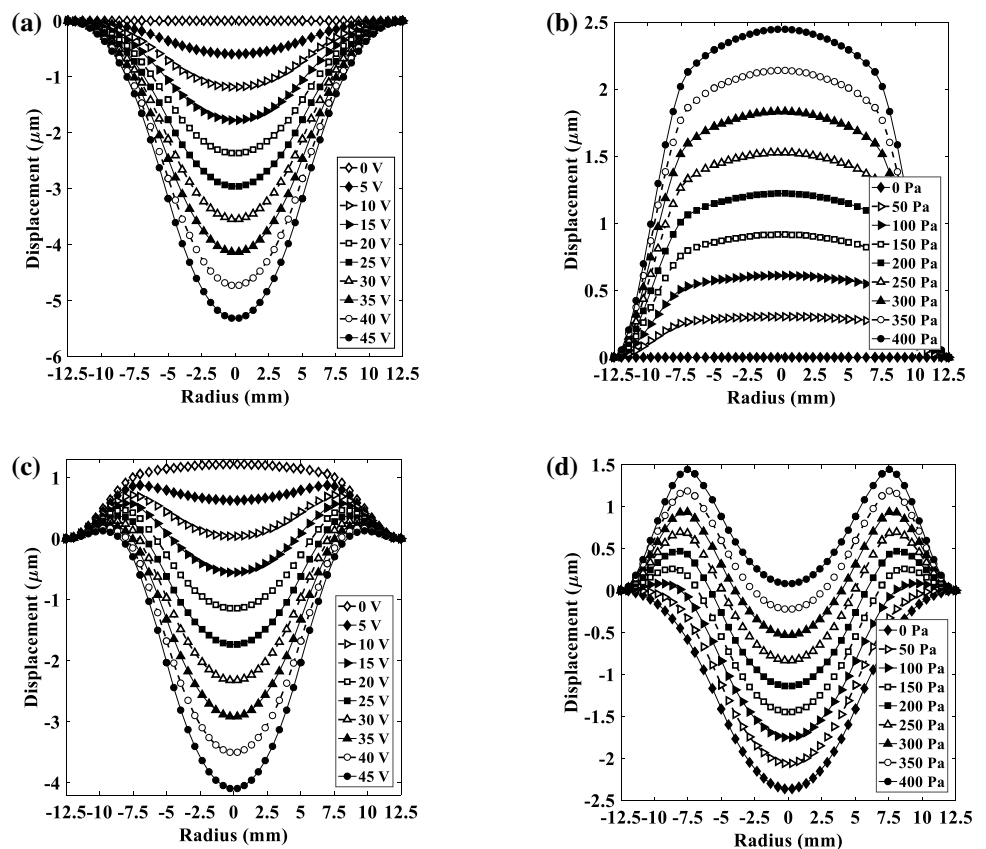
midpoint of the silicon diaphragm was obtained by analytical, FEM and experimental methods as seen in Fig. 6d. DC input voltage at 0 Hz frequency and uniform pressure load of 0 Pa were used to compare the analytical, FEM and experimental displacements of the MCPA. Because the 5 Hz actuator frequency was relatively small, it was closer to the static displacement result. It shows that the analytical, FEA and experimental results are very close each other and have acceptable similar trends. Due to the environmental conditions and the presence of environmental disturbances, slight differences have occurred in the experimental results related to FEM and analytical results.

While there was no uniform pressure, the displacement of the midline of the silicon layer at different voltages (0–45 V) is given in Fig. 7a. When the input voltage was zero, the displacement of the midline of the silicon layer under pressure loads of 0–400 Pa is given in Fig. 7b. As expected, the silicon layer remains completely horizontal in a completely unloaded state (0 Pa and 0 V). The displacement increases with increase in the voltage and pressure. The maximum displacement occurred at 45 V, and it was 5.3146 μm at the midpoint of silicon diaphragm. The displacement of the midline of the silicon layer at 5–45 V and the diaphragm exposed to 200 Pa constant fluid pressure load are given in Fig. 7c. While the displacement up to 10 V electrical load is in positive direction, the displacement of the midline of

the silicon for electric loads higher than 10 V increases in a negative direction. Note that the displacement of the exterior annulus portion of the diaphragm was less than that of the middle annulus and interior core portion. The displacement of the midline of the silicon layer under fluid pressure of 0–400 Pa and 20 V constant voltage load is given in Fig. 7d. The interior displacement decreases as fluid pressure increases, and the middle core and exterior annulus displacement increase positively.

The displacement of the midpoint of the silicon layer for different voltage and pressure loads is presented in Fig. 8. As shown in both figures, the displacement of the midpoint changes linearly in all load conditions with increasing voltage or pressure. At a certain point, when the voltage and pressure loads are equal or very close to each other, the silicon layer remains fully horizontal and the midpoint displacement is zero. The minimum flow is obtained when the PZT voltage load and fluid pressure loads acting on the silicon layer are equal or close to each other. As the pressure load increases under constant voltage loads, firstly, the centre-point displacement decreases up to reference plane. As the pressure continues to increase when the midpoint is in the horizontal position, the midpoint displacement starts to increase upwards in the positive direction. The PZT actuator cannot overcome the fluid pressure, so no pumping operation is performed (see Fig. 8a). As the voltage increases under

Fig. 7 The displacements of the midline of the silicon layer at **a** 0–45 V for 0 Pa, **b** 0–400 Pa for 0 V, **c** 0–45 V for 200 Pa and **d** 0–400 Pa for 20 V

Fig. 8 Midpoint displacements of the silicon diaphragm as a function of **a** pressure and **b** voltage
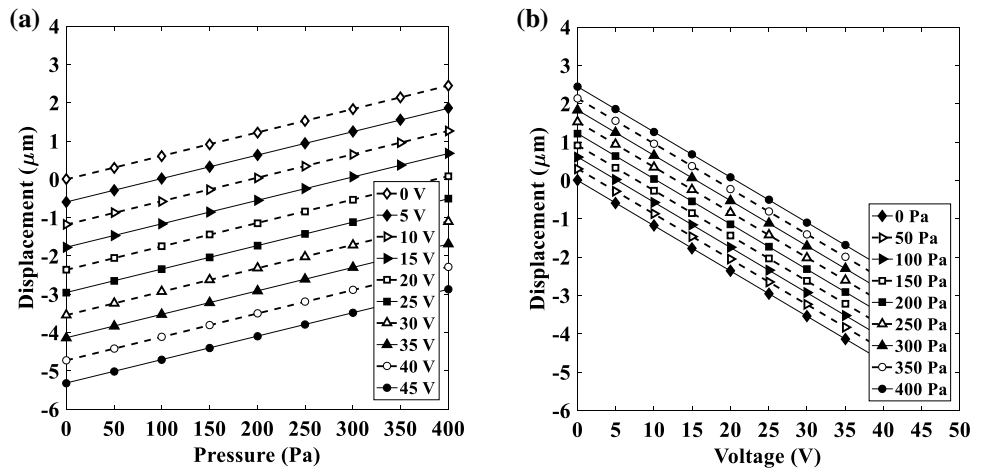

constant pressure loads, firstly, the centre-point displacement decreases up to reference plane, and therefore, the suction mode is reduced. As the voltage continues to increase while the midpoint is in the horizontal position, the displacement of the midpoint starts to increase. As the ratio of the voltage load of the PZT actuator to the fluid pressure increases, the pumping operation begins to improve (see Fig. 8b). In our previous study, net flow rate results were given and discussed in Dereshgi et al. (2020b). These results show that the most suitable values of the pressure and voltage loads should be selected for obtained maximum flow rate.

It has been determined that silicon layer thickness has a significant effect on actuator performance (Fig. 9). As the silicone layer thickness increases with respect to the PZT layer thickness, the actuator flow rate decreases nonlinearly (Fig. 9a). For the ratio $t_s/t_{pzt} \geq 1$, the actuator flow rate approaches zero. Similarly, in cases where the silicone layer thickness is smaller than the brass layer thickness, the actuator flow rate also decreases nonlinearly (Fig. 9b). However, as the elastic layer thickness increases, the stiffness of the elastic layer increases as well. As the silicone layer thickness

increases, the material stiffness increases, so the MCPA stiffness decreases also. The fact that the silicon thickness is as thin as possible compared to the PZT and brass layer thickness contributes positively to the actuator performance and flow rate increase (Fig. 9a, b). However, as the elastic layer thickness decreases, its strength and stability will decrease as well. Therefore, it should be noted that the silicon layer thickness according to PZT or brass layer thickness should not be too small. In this sense, the addition of silicon layer in piezoelectric actuators increases the actuator performance.

The effect of silicone layer thickness on the actuator centre-point displacement under 50 Pa constant uniform pressure and various voltage loads are given in Fig. 10. As the silicone layer thickness increases with respect to PZT and brass layer thickness up to $t_s/t_{pzt} \leq 0.5$, the displacement of the actuator centre point decreases nonlinearly. After the $t_s/t_{pzt} \geq 0.5$, MCPA midpoint displacements begin to decrease. After the $t_s/t_{pzt} \geq 0.8$ and $t_s/t_{br} \geq 0.8$ values of thickness ratios, there is no significant change in the amount of actuator displacement (Fig. 10a, b) It is understood that the most suitable layer thickness ratios should be around 0.8.

Fig. 9 The actuator flow rates at 50 Pa pressure and different voltages according to **a** the ratio of the PZT layer thickness to the silicone layer thickness, **b** the ratio of the brass layer thickness to the silicone layer thickness
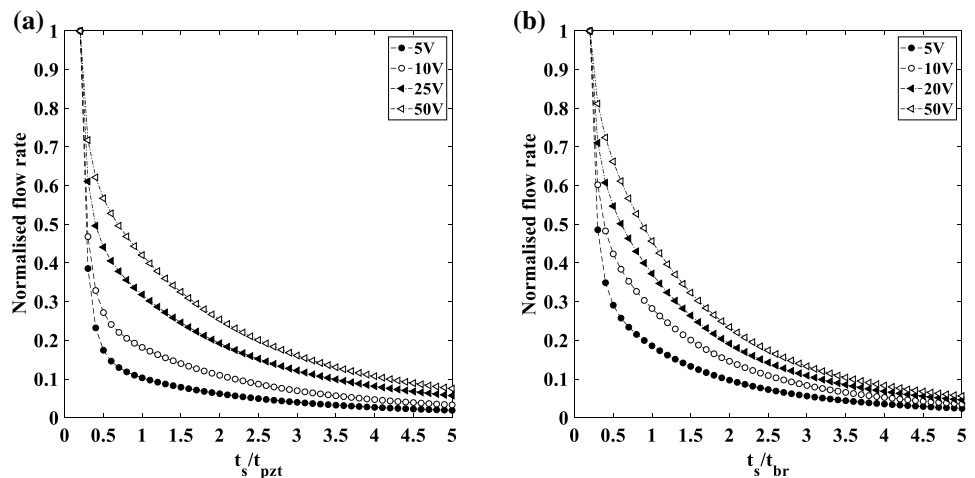
Fig. 10 Displacements of the actuator midpoint at 50 Pa and different voltages according to **a** the ratio of the PZT layer thickness to the silicone layer thickness, **b** the ratio of the brass layer thickness to the silicone layer thickness
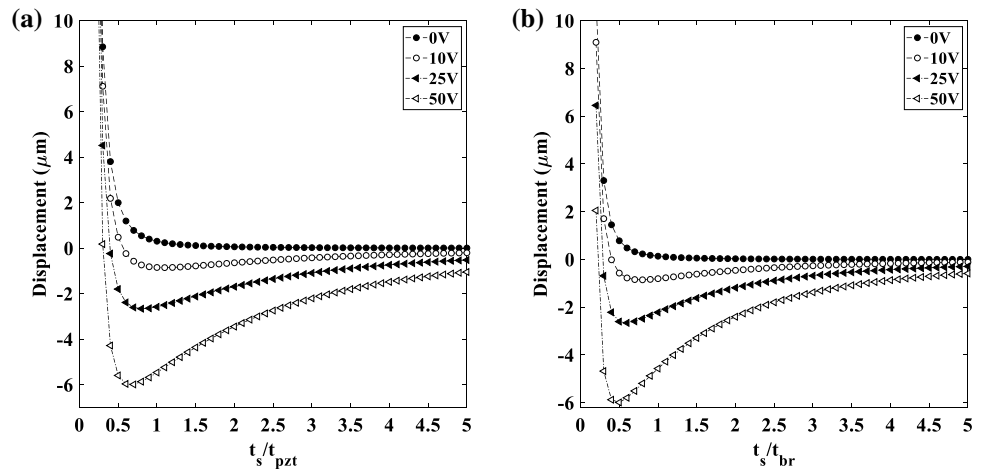
The displacement behaviour of the actuator exposed to 50 Pa constant uniform pressure and constant 10 V constant voltage load are presented in Fig. 11 for various diameter ratios. As the brass layer diameter approaches the silicon layer diameter (from $R_m/R_o = 0.56$ to $R_m/R_o \cong 0.8$), the amount of displacement increases. However, if this ratio is about 0.8, it starts to decrease again (Fig. 11a). This indicates that the ratio of brass layer diameter to silicon layer diameter should be chosen around $R_m/R_o \cong 0.8$ for best actuator performance and flow rate. As the PZT layer diameter approaches the brass layer diameter (from $R_i/R_m = 0.71.43$ to $R_i/R_m = 1$), the amount of displacement increases (Fig. 11b). Because, as the PZT layer diameter increases, the electric field intensity increases, the PZT material can produce more bending moment. However, the displacement increases as we approach the actuator centre, while it decreases as the actuator approaches the edge points fixed.

The effect of bonding layers connecting the layers to actuator performance is examined in Fig. 12. It is understood that the effect of bonding layer is very important for the actuator exposed to 50 Pa constant uniform pressure and

10 V constant voltage load. Depending on the applied pressure and voltage load, bonding with a thickness of 10% of the silicon layer thickness reduces the actuator displacement performance by about 5%. In calculations, it is important to take into account the effects of the bonding layer. For precise micropump designs, applying the actuator's bonding layer as thin as possible will have a positive effect on MCPA flow rate and performance.

4 Conclusion

In this study, the effect of electromechanical factors for the static displacement performance of a MCPA diaphragm used for pumping fluid in micropumps was investigated. The proposed actuator model consists of structures with 3 different diameters and 7 layers. The MCPA was in the form of three main layers containing silicon, brass and the PZT layer, 2 laminated layers with 2 epoxy, 4 additional layers containing 2 silver, and 2 partially covered circular plates. Analytical displacement function, which is a function of uniform pressure and voltage, was obtained by

Fig. 11 Displacement of the actuator midline for 50 Pa and 10 V according to **a** the ratio of brass layer diameter to the silicon layer diameter, **b** the ratio of the PZT layer diameter to the brass layer diameter
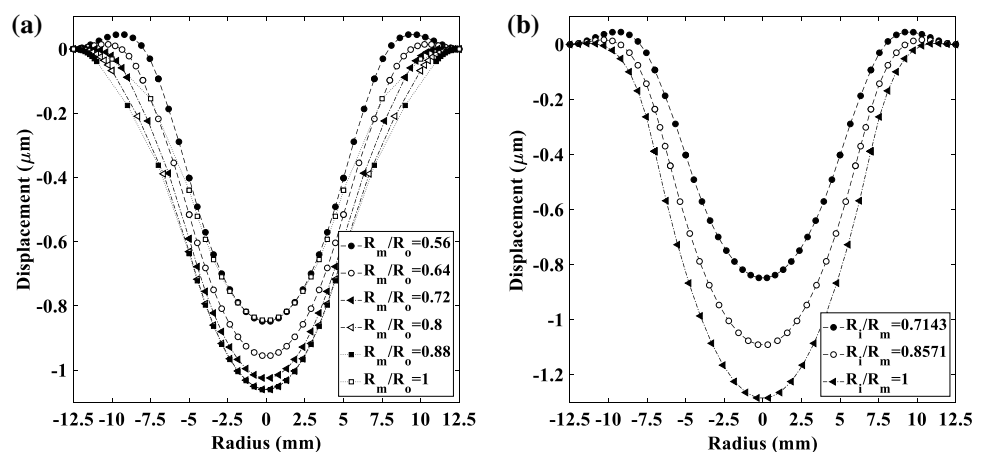
Fig. 12 Effect of the bounding layer on the actuator performance for 50 Pa and 50 V, **a** the displacements of the midline for the different for different t_{bo}/t_s thickness ratios, **b** the displacements of the midpoint according to thickness ratios t_{bo}/t_s
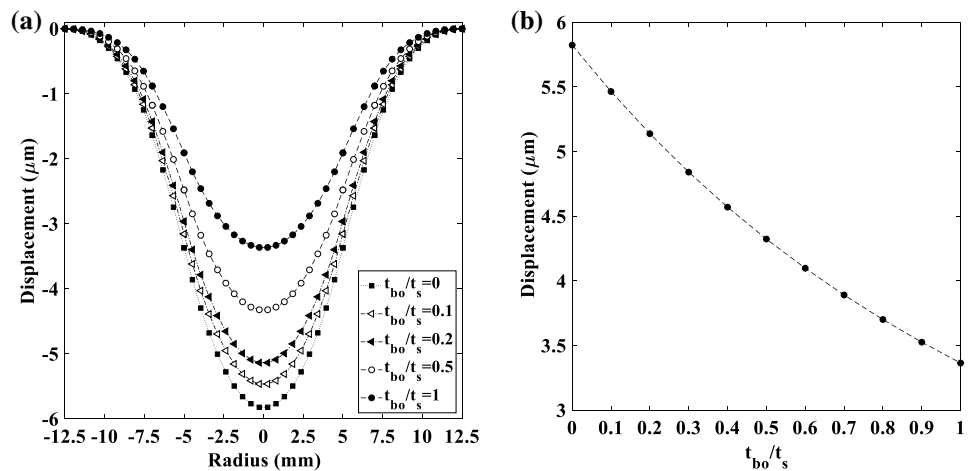
using CLPT to examine the static displacement behaviour of silicon-containing MCPA. Fourth-order partial differential equations derived from moment equilibrium equations of the actuator model were solved together with lateral and transverse displacement expressions. Transverse and lateral displacement functions were obtained depending on voltage, pressure and physical and mechanic properties. Analytical displacement model was confirmed by experimental tests and finite element analysis results. The effects of the physical properties of the pressure, voltage and actuator layers on the static displacement performance and flow rate were discussed through the obtained analytical model. It was observed that the actuator displacement increases linearly as the voltage load increases, and the actuator displacement decreases linearly as the pressure increases. As the thickness of the silicone layer increases according to PZT and brass layer thicknesses, the amount of fluid pumped decreases. For best actuator performance, the ratio of silicon layer thickness to PZT and brass layer thickness should be 0.8 and brass layer diameter to silicon layer diameter should be approximately 0.8. Also, the PZT layer diameter increases the static displacement performance of the MCPA. It has been determined that the bounding layer reduces the amount of static displacement by approximately 5%.

It has been determined how this MCPA is affected by electromechanical parameters by extensive analyses. Obtained analytical displacement model can be used for optimization and improvement of micropump performance and in the designing diaphragm type in MCPA of micropumps. All in all, the results showed that MCPA would be a good candidate for biomedical application micropumps.

References

Abhari F, Jaafar H, Yunus NAM (2012) A comprehensive study of micropumps technologies. Int J Electrochem Sci 7:9765–9780

Afrasiab H, Movahhedy M, Assempour A (2011) Proposal of a new design for valveless micropumps. Sci Iran 18:1261–1266. https://doi.org/10.1016/j.scient.2011.11.023

Callister WD, Rethwisch DG (2015) Materials science and engineering: SI version. Wiley, New York

Chee PS, Nafea M, Leow PL, Ali MSM (2016) Thermal analysis of wirelessly powered thermo-pneumatic micropump based on planar LC circuit. J Mech Sci Technol 30:2659–2665. https://doi.org/10.1007/s12206-016-0527-5

Cheong HR, Lai KC, Chee PS (2018) A wireless powered electroactive polymer using magnetic resonant coupling. IOP Conf Ser Mater Sci Eng. https://doi.org/10.1088/1757-899x/409/1/012002

Cho J, Anderson M, Richards R, Bahr D, Richards C (2005) Optimization of electromechanical coupling for a thin-film PZT membrane: II. Experiment. J Micromech Microeng 15:1804–1809. https://doi.org/10.1088/0960-1317/15/10/003

Dereshgi HA (2016) Design of novel micro-pumps for mechatronic applications. In: International symposium on innovative technologies in engineering and science (ISITES), pp 1435–1447

Dereshgi HA (2019) Investigation of electromechanical factors effecting micro-pump characteristics for biomedical applications. Ph.D. thesis, Sakarya University

Dereshgi HA, Yildiz MZ (2018a) Investigation of electro-mechanical factors effecting piezoelectric actuator for valveless micropump characteristics. J Eng Sci Technol 13:2843–2856

Dereshgi HA, Yildiz MZ (2018b) A novel micropump design: investigation of the voltage effect on the net flow rate. Sakarya Univ J Sci 22:1152–1156. https://doi.org/10.16984/saufenbilder.388658

Dereshgi HA, Yildiz MZ (2019) Numerical study of novel MEMS-based valveless piezoelectric micropumps in the range of low voltages and frequencies. In: Scientific meeting on electrical-electronics & biomedical engineering and computer science (EBBT). https://doi.org/10.1109/ebbt.2019.8741629

Dereshgi HA, Dal H, Sayan ME (2020a) Analytical analysis of a circular unimorph piezoelectric actuator in the range of low voltages and pressures. Microsyst Technol. https://doi.org/10.1007/s00542-020-04786-w

Dereshgi HA, Yildiz MZ, Parlak N (2020b) Performance comparison of novel single and bi-diaphragm PZT based valveless micropumps. J Appl Fluid Mech 13:401–412. https://doi.org/10.29252/jafm.13.02.30347

Deshpande M, Saggere L (2007) An analytical model and working equations for static deflections of a circular multi-layered diaphragm-type piezoelectric actuator. Sens Actuators A Phys 136:673–689. https://doi.org/10.1016/j.sna.2006.12.022

Doll A, Goldschmidtboeing F, Heinrichs M, Woias P, Schrag HJ, Hopt UT (2004) A piezoelectric bidirectional micropump for a medical application. Fluids Eng. https://doi.org/10.1115/imece2004-61083

Dong S, Uchino K, Li L, Viehland D (2007) Analytical solutions for the transverse deflection of a piezoelectric circular axisymmetric unimorph actuator. IEEE Trans Ultrason Ferroelectr Freq Control 54:1240–1248. https://doi.org/10.1109/TUFFC.2007.377

Guerine A, Merzouki T, Hami AE, Zineb TB (2018) Uncertainty analysis of an actuator for a shape memory alloy micro-pump with uncertain parameters. Adv Eng Softw 122:22–30. https://doi.org/10.1016/j.advengsoft.2018.02.011

He X, Xu W, Lin N, Uzoejinwa BB, Deng Z (2017) Dynamics modeling and vibration analysis of a piezoelectric diaphragm applied in valveless micropump. J Sound Vib 405:133–143. https://doi.org/10.1016/j.jsv.2017.05.025

Hu Y, Liang X, Wang W (2017) A theoretical solution of resonant circular diaphragm-type piezoactuators with added mass loads. Sens Actuators A Phys 258:74–87. https://doi.org/10.1016/j.sna.2017.02.029

Jang J, Lee SS (2000) Theoretical and experimental study of MHD (magnetohydrodynamic) micropump. Sens Actuators A Phys 80:84–89. https://doi.org/10.1016/s0924-4247(99)00302-7

Kaviani S, Bahrami M, Esfahani AM, Parsi B (2014) A modeling and vibration analysis of a piezoelectric micro-pump diaphragm. CR Mec 342:692–699. https://doi.org/10.1016/j.crme.2014.06.005

Kim JH, Kang C, Kim YS (2004) A disposable polydimethylsiloxane-based diffuser micropump actuated by piezoelectric-disc. Microelectron Eng 71:119–124. https://doi.org/10.1016/j.mee.2003.10.005

Kolahdouz EM, Mohammadzadeh K, Shirani E (2014) Performance of piezoelectrically actuated micropump with different driving voltage shapes and frequencies. Sci Iran 21:1635–1642

Li S, Chen S (2003) Analytical analysis of a circular PZT actuator for valveless micropumps. Sens Actuators A: Phys 104:151–161. https://doi.org/10.1016/s0924-4247(03)00006-2

Maillefer D, Lintel HV, Rey-Mermet G, Hirschi R (1999) A high-performance silicon micropump for an implantable drug delivery system. In: IEEE international conference on microelectromechanical systems. https://doi.org/10.1109/memsys.1999.746886

Mo C, Wright R, Slaughter WS, Clark WW (2006) Behaviour of a unimorph circular piezoelectric actuator. Smart Mater Struct 15:1094–1102. https://doi.org/10.1088/0964-1726/15/4/023

Mohammadi S, Abdalbeigi M (2013) Analytical optimization of piezoelectric circular diaphragm generator. Adv Mater Sci Eng 2013:1–10. https://doi.org/10.1155/2013/620231

Monemian Esfahani A, Bahrami M (2016) Vibration analysis of a circular thin polymeric piezoelectric diaphragm with fluid interaction. Int J Mech Mater Design 12:401–411. https://doi.org/10.1007/s10999-015-9308-z

Monemian Esfahani A, Bahrami M, Ghaffarian Anbarani SR (2018) Forced transverse vibration analysis of a circular viscoelastic polymeric piezoelectric microplate with fluid interaction. Aust J Mech Eng 16:31–42. https://doi.org/10.1080/14484846.2017.1294520

Munas FR, Amarasinghe YWR, Dao D (2015) Review on MEMS based micropumps for biomedical applications. Int J Innov Res Sci Eng Technology 4:5602–5615

Nisar A, Afzulpurkar N, Mahaisavariya B, Tuantranont A (2008) MEMS-based micropumps in drug delivery and biomedical applications. Sens Actuators B: Chem 130:917–942. https://doi.org/10.1016/j.snb.2007.10.064

Olfatnia M, Singh VR, Xu T, Miao JM, Ong LS (2010) Analysis of the vibration modes of piezoelectric circular microdiaphragms. J Micromech Microeng. https://doi.org/10.1088/0960-1317/20/8/085013

Oniszczuk Z (1999) Transverse vibrations of elastically connected rectangular double-membrane compound system. J Sound Vib 221:235–250. https://doi.org/10.1006/jsvi.1998.1998

Pan LS, Ng TY, Liu GR, Lam KY, Jiang TY (2001) Analytical solutions for the dynamic analysis of a valveless micropump—a fluid-membrane coupling study. Sens Actuators, A 93:173–181. https://doi.org/10.1016/S0924-4247(01)00638-0

Ramesh K, Tripathi D, Bég OA, Kadir A (2019) Slip and hall current effects on Jeffrey fluid suspension flow in a peristaltic hydromagnetic blood micropump. Iran J Sci Technol Trans Mech Eng 43:675–692. https://doi.org/10.1007/s40997-018-0230-5

Rusli M, Chee PS, Arsat R, Lau KX, Leow PL (2018) Electromagnetic actuation dual-chamber bidirectional flow micropump. Sens Actuators A: Phys 282:17–27. https://doi.org/10.1016/j.sna.2018.08.047

Singhal V, Garimella SV (2007) Induction electrohydrodynamics micropump for high heat flux cooling. Sens Actuators A: Phys 134:650–659. https://doi.org/10.1016/j.sna.2006.05.007

Tripathi D, Sharma A, Bég OA (2017) Electrothermal transport of nanofluids via peristaltic pumping in a finite micro-channel: effects of Joule heating and Helmholtz–Smoluchowski velocity. Int J Heat Mass Transf 111:138–149. https://doi.org/10.1016/j.ijheatmasstransfer.2017.03.089

Uhlig S, Gaudet M, Langa S, Schimmanz K, Conrad H, Kaiser B et al (2018) Electrostatically driven in-plane silicon micropump for modular configuration. Micromachines 9:190. https://doi.org/10.3390/mi9040190

Wang YN, Fu LM (2018) Micropumps and biomedical applications—a review. Microelectron Eng 195:121–138

Wang DH, Huo J (2010) Modeling and testing of the static deflections of circular piezoelectric unimorph actuators. J Intell Mater Syst Struct 21:1603–1616. https://doi.org/10.1177/1045389X10385485

Wang X, Cheng C, Wang S, Liu S (2009) Electroosmotic pumps and their applications in microfluidic systems. Microfluid Nanofluid 6:145–162. https://doi.org/10.1007/s10404-008-0399-9

Yang J (2006) Analysis of piezoelectric devices. World Scientific, Hackensack

Yildiz MZ, Dereshgi HA (2019) Design and analysis of PZT micropumps for biomedical applications: glaucoma treatment. J Eng Res 7:202–217

Yong YK, Ahmed B, Moheimani SOR (2010) Atomic force microscopy with a 12-electrode piezoelectric tube scanner. Rev Sci Instrum 81(3):033701. https://doi.org/10.1063/1.3314901

Yu M, Balachandran B (2005) Sensor diaphragm under initial tension: linear analysis. Exp Mech 45:123–129. https://doi.org/10.1177/0014485105052319

Zordan E, Amirouche F, Zhou Y (2009) Principle design and actuation of a dual chamber electromagnetic micropump with coaxial cantilever valves. Biomed Microdev 12:55–62. https://doi.org/10.1007/s10544-009-9358-9